Astronomy & Astrophysics manuscript no. Paper1˙aa
February 20, 2012
© ESO 2012

arXiv:1202.3829v1 [astro-ph.EP] 17 Feb 2012

LETTER TO THE EDITOR

Secondary eclipse scanning of HD 189733b: The perspectives of mapping distant worlds

Julien de Wit[1,2], Michaël Gillon[3], Brice-Olivier Demory[1], and Sara Seager[1,4]

[1] Department of Earth, Atmospheric and Planetary Sciences, MIT, 77 Massachusetts Avenue, Cambridge, MA 02139, USA. e-mail: jdewit@mit.edu
[2] Faculté des Sciences Appliquées, Université de Liège, Grande Traverse 12, 4000 Liège, Belgium.
[3] Institut d'Astrophysique et de Géophysique, Université de Liège, Allée du 6 Août 17, 4000 Liège, Belgium.
[4] Department of Physics and Kavli Institute for Astrophysics and Space Research, MIT, 77 Massachusetts Avenue, Cambridge, MA 02138, USA.

Received ; accepted

ABSTRACT

Context. Mapping the brightness distribution of exoplanets is the next frontier for exoplanet infrared photometry studies. For tidally-locked hot Jupiters that transit and are eclipsed by their host star with non-zero impact parameter, the first steps are now possible.
Aims. The aim is to use eclipse scanning from occultation ingress/egress and phase curve measurements to constrain exoplanet large-scale brightness structure.
Methods. We use archived *Spitzer*/IRAC 8 μm data of HD 189733 in a global MCMC procedure encompassing six transits, eight secondary eclipses, and a phase curve in a two-step analysis. The first step derives the planet-star system parameters. The second step investigates the structure found in eclipse scanning, using the previous planet-star system parameter derivation as Gaussian priors.
Results. We find a 5-σ deviation from the expected occultation ingress/egress shape for a uniform brightness disk, and demonstrate that this is dominated by large-scale brightness structure and not an occultation timing offset due to a non-zero eccentricity. Our analysis yields a 2D brightness temperature distribution showing a large-scale asymmetric hot spot whose finer structure is limited by the data quality and planet orbit geometry. We also present an improved upper limit for eccentricity, $e \leq 0.0081$ (95% confidence).
Conclusions. Reanalysis of archived HD 189733 data revealed brightness structure by using global analysis that mitigated systematics. Future eclipse scanning observations of the same exoplanet at other wavelengths will probe different atmosphere layers, ultimately generating a large-scale 3D map.

Key words. eclipses – planets and satellites : individual : HD 189733b – techniques : (photometric)

1. Introduction

Among the hundreds exoplanets detected to date[1], it is the subset of transiting exoplanets that can be most extensively characterized with current technology. Beyond derivation of the exoplanet orbital inclination and density (e.g., Winn 2010), transiting planets are key objects because their atmospheres are observationally accessible through transit transmission and occultation emission spectrophotometry (see e.g., Seager & Deming 2010, and references therein). In addition, exoplanet phase-dependent infrared flux modulations provide observational constraints on the exoplanet atmosphere properties; from phase curve IR measurements, Knutson et al. (2007) derived the first longitudinal brightness distribution of an exoplanet. This longitudinal map indicated a hot spot within the exoplanet atmosphere, in particular an offset hot spot in agreement with predicted super-rotating equatorial jet for hot Jupiters (e.g., Showman & Guillot 2002). Related, significant theoretical developments have also been achieved in modeling exoplanet atmospheric hydrodynamic flow with radiative transfer (e.g., Showman et al. 2009; Rauscher & Menou 2010; Dobbs-Dixon et al. 2010; Moses et al. 2011).

The observation of localized, specific spatial features, such as hot spots or cold vortices, is essential for constraining atmospheric structure that arises from complex hydrodynamic processes. Eclipses have proved to be powerful tools for "spatially resolving" distant objects, including binary stars (e.g., Warner et al. 1971) and accretion disks (e.g., Horne 1985). Previous theoretical studies introduced the potential of eclipse scanning[2](see Figure 1) for exoplanets in order to disentangle atmospheric circulation regimes (e.g., Williams et al. 2006; Rauscher et al. 2007). In the first direct mention of eclipse scanning, Agol et al. (2010) detected the "uniform time offset" (defined by Williams et al. 2006, see our Subsection 2.2) expected for the HD 189733b hot spot based on the longitudinal map derived by Knutson et al. (2007).

Ideally a tidally-locked transiting and occulted exoplanet with a non-zero impact parameter can enable a coarse 2D surface brightness map. As represented in Figure 1, such an exoplanet is scanned through several processes along its orbit. During occultation ingress/egress, the planet is gradually masked/unmasked by its host star. In addition, one may derive the flux in longitudinal slices from the phase curve as the planet revolves around the star, as long as the exoplanet is tidally locked. The three different scanning components (ingress, egress, phase curve) provide us with complementary pieces of information that could ul-

[1] For an up-to-date list see the Extrasolar Planets Encyclopaedia: http://exoplanet.eu

[2] Eclipse scanning is the process by which a body gradually masks another body.

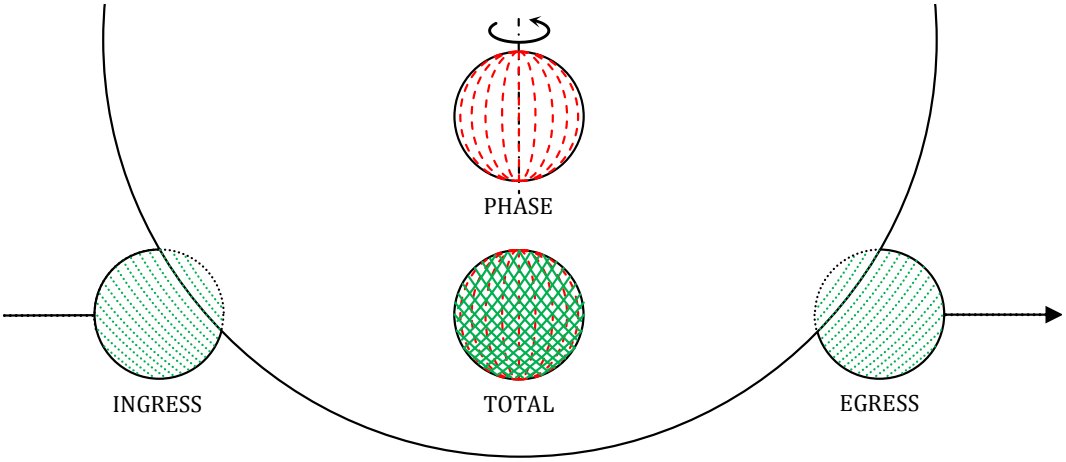

Fig. 1. Schematic description of the different scanning processes observable for a occulted exoplanet.

timately lead to determine the brightness distribution over a specific "grid" (e.g., see the component labeled "*total*" in Figure 1).

Exoplanet thermal infrared observations aiming at characterizing planetary brightness distribution are growing. Currently, *Spitzer* has observed thermal phases curves for eight different exoplanets as well as the infrared occultations of over two dozen exoplanets. Among these, HD 189733b (Bouchy et al. 2005) is arguably the most favorable transiting planet for detailed observational atmosphere studies: its K star is the closest to Earth with a transiting hot Jupiter. This means the star is bright and the eclipses are relatively deep yielding favorable SNR datasets. As such, HD 189733b represents a "Rosetta Stone" for the field of exoplanetology with: one of the highest SNR secondary eclipses (Deming et al. 2006; Charbonneau et al. 2008); phase curve observations (Knutson et al. 2007, 2009); numerous atmospheric observational characterizations (e.g., Grillmair et al. 2007; Tinetti et al. 2007; Redfield et al. 2008; Swain et al. 2008; Madhusudhan & Seager 2009; Désert et al. 2009; **?**; Deroo et al. 2010). Although HD 189733b atmospheric models are in qualitative agreement with observations, important discrepancies remain between simulated and observed light curves as well as emission spectra (see e.g., Showman et al. 2009).

We undertake a consistent and global analysis of all HD 189733b public photometry obtained with the *Spitzer Space Telescope* (Werner et al. 2004) to assess the validity of published inferences and detect effects that would remain unnoticed in the frame of individual data sets analysis (de Wit et al., in prep). In this paper, we present the first eclipse scanning with a detection of an occultation ingress/egress deviation from a uniform brightness disk at the 5-σ level. However, the brightness determination over a specific grid (see Figure 1) is not yet obtainable because 1) the data is not of high quality enough: there will be no significance on a grid cell and 2) to make a 2D map a higher level of precision of the system parameters is needed. In particular for the eccentricity that is highly degenerated with the brightness distribution. For that reason we proposed another procedure to constrain consistently the eccentricity-brightness degeneracy. The main point of the paper is our new procedure on how to handle the eccentricity-brightness distribution degeneracy and what features in a 2D surface brightness distribution can be identified. In particular, we simultaneously derive the dominant two-dimensional pattern of HD 189733b's atmosphere and a highly precise upper limit on its orbital eccentricity, by combining the occultation ingress/egress deviation detection with the phase-curve from Knutson et al. (2007).

At the time of submission, we learned about a similar work by Majeau et al. (2012), hereafter M12, focusing on the derivation of HD 189733b 2D eclipse map, using the same data set but a different data analysis. In contrast to M12 who present a 2D map, we focus on the dominant 2D surface brightness patterns, because finding a unique 2D map requires higher quality data than available. Furthermore, we present a 5-σ deviation from the expected occultation ingress/egress shape for a uniform brightness disk, a critical component in deriving the 2D dominant brightness pattern. Our work differs from M12 in two ways. First, a significant point is that the planet surface brightness distribution is degenerate with planet orbital eccentricity which is not measured. Our work highly constrains this degeneracy. Second, and related to the first point, we propagate the system parameter uncertainty as it affects the precision to which the 2D surface brightness patterns can be derived. We further discuss a comparison of the techniques and results in Sec. 4.

We begin with a summary description of the 8 μm *Spitzer* data sets. In Subsection 2.1 we present our photometric data analysis and the occultation ingress/egress deviation from a uniform brightness disk. In Subsection 2.2, we investigate the possible origins of the ingress/egress structure and describe our procedure for consistently disentangleing the causes. We present our results in Section 3, including the HD 189733b brightness distribution at 8 μm and a precise eccentricity upper limit. Then we discuss the robustness of our detection and the necessity of global analysis to mitigate the impacts of systematics, to both enable detection of previously unnoticed effects and constrain degeneracies. We conclude by discussing the implications for measuring the dominant 3D brightness features: each wavelength corresponds to a different atmospheric layer in altitude and so combining 2D results at different wavelengths can lead to an extraction of 3D map features, highlighting tremendous potential for resolving distant worlds.

2. Data Analysis

We divide our work in two major steps. First, we perform a global determination of the system parameters (the orbital and physical parameters of the star and planet) based on the IRAC 8 μm transit and occultation photometry. The parameter determination lead to our detection of anomalous ingress/egress shapes that are presented at the end of Subsection 2.1. Using the system parameter estimates as Gaussian priors, we simultaneously

analyze the 8 μm *Spitzer* IRAC photometry of HD 189733, including occultation and phase curve photometry.

2.1. System Parameters Estimation

2.1.1. Data description and reduction

The eight secondary eclipses and the six transits of HD189733b used in our system parameter estimation are listed in Table 2. The data was obtained from November 2005 to June 2008 with the *Infrared Array Camera* (IRAC: Fazio et al. 2004) at 8 μm. The data[3] used in this study, calibrated by the *Spitzer* pipeline version S18.18.0, are described (by *Astronomical Observation Requests*, hereafter AOR) in Table 2. The new S18.18.0 version enables improvements in the quality of data reduction over the original published data sets which used older *Spitzer* pipeline versions[4].

The data reduction follows conventional procedures (e.g., Gillon et al. 2010b, hereafter G10, and references therein) and is performed individually and consistently for each AOR (de Wit et al., in prep). For each AOR, we first convert fluxes from the *Spitzer* units of specific intensity (MJy/sr) to photon counts, then perform aperture photometry on each image with the `IRAF`[5] `/DAOPHOT` software (Stetson 1987). We estimate the best aperture radius (see Table 2) based on the instrument point-spread function (PSF[6]), HD189733b's, its host star and the background contributions. We estimate the PSF center by fitting a Gaussian profile to each image. A mean sky background is measured in an annulus extending from 10 to 16 pixels from the PSF center, and subtracted from the measured flux of each frame. We discard the first 30 minutes of the data to allow detector stabilization. According to the *x*-*y* distribution of the PSF centers we reject the few significant outliers to the bulk of the distribution. For each set of 64 subarray images, we discard measurements with discrepant values of flux, background and PSF center positions using a 10σ median clipping. The resulting flux values are averaged across each set of 64 subarray images and we take the photometric error as the error on the average flux measurement.

2.1.2. Photometry data analysis

We now describe the procedure we use to analyze the eight occultations and six transits obtained in IRAC 8 μm channel in order to constrain HD 189733b system parameters (see Table 2). We emphasize that we simultaneously analyze the whole data set in what we term a "global analysis", instead of combining the each separately analyzed transit or eclipse events. The global analysis approach helps to mitigate the impacts of systematics and therefore enables detection of previously unnoticed effects in the data. For this first part of the analysis, we model the exoplanet as a disk of uniform brightness distribution.

We use an adaptive Markov Chain Monte Carlo (MCMC; see e.g. Gregory 2005; Ford 2006) algorithm. MCMC is a Bayesian inference method based on stochastic simulations that sample the posterior probability distribution of adjusted parameters for a given model. We use here the implementation presented in detail in Gillon et al. (2009, 2010a,b). More specifically, this implementation uses Keplerian orbits and models the eclipse photometry using the model of Mandel & Agol (2002) multiplied by a baseline, different for each time-series, to take into account the systematics (see below).

Eclipse model & limb-darkening

We model the secondary eclipse assuming the planet to be a uniform disk, and the transit assuming a quadratic limb-darkening law. We draw the limb-darkening coefficients from the theoretical tables of Claret & Bloemen (2011), $u_1 = 0.0467 \pm 0.0009$ and $u_2 = 0.0979 \pm 0.0015$, based on the spectroscopic parameters of HD 189733 ($T_{eff} = 5050 \pm 50K$, $\log g = 4.61 \pm 0.03$ and $[\frac{Fe}{H}] - 0.03 \pm 0.05$, see Southworth 2010, and references therein). We add this a priori knowledge, using as additional jump parameters[7] the combinations $c_1 = 2u_1 + u_2$ and $c_2 = u_1 - 2u_2$, as a Bayesian penalty to our merit function as described in G10. The impact of this coefficient choice does not affect our results (see Sec. 3).

Systematics

IRAC instrumental systematics variation of the observed flux, such as pixel-phase or detector ramp, are well-documented (e.g., Désert et al. 2009, and references therein). At 8 μm, Si:As-based detector showed a uniform intrapixel sensitivity (i.e. negligible pixel-phase effect) but temporal evolution of their pixels gain (detector ramp). Following Charbonneau et al. (2008) we model locally the detector ramp as a quadratic function of $ln(dt)$. In addition, we take into account known low-frequency noise sources (instrumental and stellar) with a second order time-dependent polynomial.

We use linear baseline models and determine their coefficients by linear least squares minimization at each step of the MCMC. For this purpose, we applied the *Singular Value Decomposition* (SVD) method (Press et al. 1992).

Correlated noise

To obtain reliable error bars on our parameters, we take into account the correlated noise following a procedure similar to Winn et al. (2008). For each light curve, we estimated the standard deviation of the best-fitting solution residuals for time bins ranging from 3.5 to 30 minutes. For each time bin, the following factor β_{red} is determined

$$\beta_{red} = \frac{\sigma_N}{\sigma_1} \sqrt{\frac{N(M-1)}{M}}, \quad (1)$$

where N is the mean number of points in each bin, M is the number of bins, and σ_1 and σ_N are respectively the standard deviation of the unbinned and binned residuals. The largest value obtained with the different time bins is used to multiply the error bars of the measurements.

[3] Data available in the form of Basic Calibrated Data (BCD) on the *Infrared Science Archive* : `http://sha.ipac.caltech.edu/applications/Spitzer/SHA//`

[4] `http://irsa.ipac.caltech.edu/data/SPITZER/docs/irac/iracinstrumenthandbook/73`

[5] IRAF is distributed by the National Optical Astronomy Observatory, which is operated by the Association of Universities for Research in Astronomy, Inc., under cooperative agreement with the National Science Foundation.

[6] `http://ssc.spitzer.caltech.edu/irac/psf.html`

[7] Jump parameters are the model parameters that are randomly perturbed at each step of the MCMC method

Table 1. Exoplanet and star parameters

Parameters (units)	Median ± 1 σ
$(R_p/R_\star)^2$	$0.023985\pm^{0.000062}_{0.000089}$
$b(R_\star)$	$0.6630\pm^{0.0032}_{0.0045}$
$P(days)$	$2.2185740\pm^{0.0000003}_{0.0000003}$
$W(days)$	$0.07513\pm^{0.00013}_{0.00013}$
$T_0(hjd-2453980)$	$8.803281\pm^{0.000066}_{0.000065}$
$F_p/F_\star\|_{8\mu m}$	$0.003432\pm^{0.000046}_{0.000046}$
$a(AU)$	$0.03143\pm^{0.00076}_{0.00072}$
$i(^\circ)$	$85.72\pm^{0.058}_{0.038}$
$\rho_\star(\rho_\odot)$	$1.905\pm^{0.037}_{0.024}$
$R_\star(R_\odot)$	$0.762\pm^{0.019}_{0.019}$
$R_p(R_J)$	$1.152\pm^{0.028}_{0.028}$

Jump parameters & priors

In our analysis, we used the following jump parameters; the planet/star area ratio $(R_p/R_\star)^2$, the orbital period P, the transit duration (from the first to last contact) W, the impact parameter $b = a/R_\star \cos i$, $\sqrt{e}\cos\omega$ and $\sqrt{e}\sin\omega$ and the time of minimum light T_0. We assumed a uniform prior distribution for all these jump parameters and draw at each step a random $M_\star$ based on the Gaussian prior: $M_\star = 0.84 \pm 0.06 M_\odot$(Southworth 2010). In this first analysis, we also constrained the eccentricity to zero (see below and Sec. 3).

2.1.3. Intermediate results

We present the system parameter estimation results here, as they are the starting point for the second analysis step focussing on HD 189733b eclipse scanning (see Subsection 2.2).

System parameters

We present the system parameters resulting from our global MCMC simulation in Table 1, by the median values and 68.3% probability interval for the jump and physical parameters. We estimate these parameters similarly to Agol et al. (2010), setting $e = 0$ based on the small inferred value of $e\cos\omega$ and theoretical predictions (see Sec. 3). We further test the incidence of the system parameter estimation based on the $e = 0$ assumption: the conclusions presented in Section 3 are similar when based on system parameters estimated with e freely varying or with e set to zero. We compute our best-fit parameters based on a global MCMC simulation of the ten AORs (see Table 2), in opposition to Agol et al. (2010) that took these as a weighted mean of individual transit or eclipse analysis. Although our global analysis is more consistent to extract the information of each AOR and thus robust to systematics, our best-fit parameters are in good agreement with Agol et al. (2010).

Eclipse scanning

We have detected structure in the HD 189733b occultation ingress/egress light curves that deviates at the 5σ level from the expected ingress/egress shape of a gradually occulted uniformly bright disk. We determine the significance of this structure as $\sqrt{\sum_{i\in ingress}\frac{Y_i}{\sigma_i} - \sum_{i\in egress}\frac{Y_i}{\sigma_i}}$, where Y_i and σ_i are the measurement and its error bar at time i. The error bars are rescaled by β_{red} (here on average of 1.3) to take into account the correlated noise effects on our detection. Figure 2 shows the IRAC photometry of the eclipses ingress/egress corrected for the systematics and binned per 1 minute, with the best-fitting eclipse model superimposed. Our detection occultation ingress/egress deviation detection is in agreement with the expected signature of the HD 189733b hot spot (Knutson et al. 2007). We explore other possible origins for this structure in Subsection 2.2.

2.2. Eclipse scanning analysis

The second part of the analysis aims on investigating the origin of the occultation ingress/egress deviation from a uniform brightness disk, i.e. the 5-σ detection of structure in the occultation ingress/egress.

2.2.1. Eclipse scanning: possible origins

The primary potential origins of the occultation ingress/egress structure detected are: (1) non-spherical exoplanet; (2) small, but non-zero, eccentricity; (3) non-uniform brightness distribution. (1) We reject the non-spherical exoplanet concept because we have detected no significant structure in transit ingress/egress (Figure 2, in particular bottom-right panel). The spherical planet finding is in agreement with current constraints on the HD 189733b oblateness (Carter & Winn 2010) and wind-driven shape (expected to introduce light-curve deviation below 10ppm, see Barnes et al. 2009). For HD 189733b shape-induced structure are expected to be about one order of magnitude larger in primary than in secondary eclipse (I_p/I_*, I_p, I_* respectively the exoplanet and the star mean intensity at 8 μm). We therefore take the planet to be spherical. (2 and 3) A non-zero eccentricity can introduce an apparent "timing offset" to the occultation of a uniform disk. This can mimic a non-uniform brightness distribution that is also expressed by structure in the occultation ingress/egress (see Williams et al. 2006). In particular for nearly circular orbits, occultations occur $\Delta t_c \approx \frac{P}{2}[1 + \frac{4}{\pi}e\cos\omega]$ after transits (see e.g., Winn 2010), leading to a biased estimation of $\sqrt{e}\cos\omega$ and $\sqrt{e}\sin\omega$ due to apparent timing offset (see Sec. 3).

Before turning to our occultation mapping we recall that exoplanet scanning involves three different components: ingress, egress and phase curve. They provide complementary pieces of information (for a tidally-locked planet with non-zero impact parameter) that could ultimately lead to a determination of the brightness distribution over a specific "grid" (see Figure 1). However a 2D map is not yet obtainable because 1) the data is not of high enough quality: there will be no significance in signal on a grid cell and 2) to make a 2D map a higher level of precision of system parameters is needed, especially for the eccentricity, than is available. Here we provide a careful analysis of the brightness distribution-eccentricity degeneracy and use that to extract dominant features in a 2D brightness distribution. The analysis also leads to confirmation that the ingress/egress brightness anomaly is real and not solely due to a timing offset from eccentricity.

2.2.2. Data analysis using a non-uniform brightness source occultation model

We turn to describe the procedure we used to constrain the eccentricity-brightness degeneracy using the complementary information from HD 189733b occultation and phase curve measurements. The data we use in this second step of the analysis are

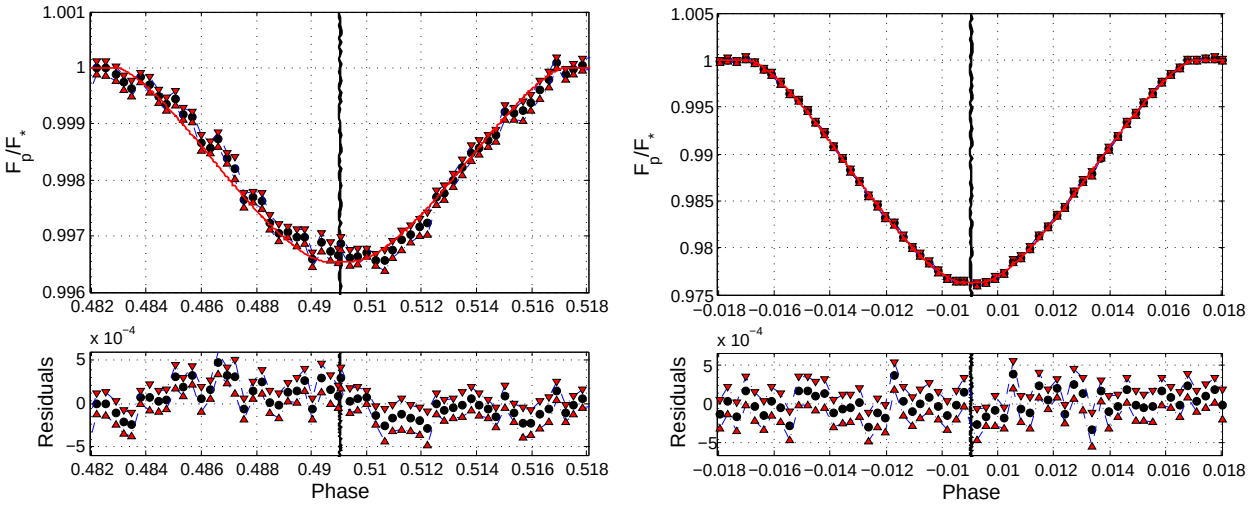

Fig. 2. IRAC 8 μm HD 189733b occultation and transit ingress/egress. **Left:** Folded occultations ingress/egress deviates from the uniform brightness disk eclipse model, highlighting the eclipse scanning of HD 189733b dayside. **Right:** Folded transits showing no significant structure during ingress/egress (i.e. no significant deviation to the transit of a perfect sphere). **Top:** Global eclipse photometry binned per 1 minute and corrected for the systematics with the best-fitting eclipse model superimposed (in red). **Bottom:** Combined residuals.

the detrended and folded occultations obtained from the first step of our analysis (from Subsection 2.1), and the phase curve from (Knutson et al. 2007) corrected for stellar variability (see Agol et al. 2010). We discard the first third of the phase curve since it is strongly affected by systematics, incl. the ramp correction.

The procedure we use to constrain the eccentricity-brightness degeneracy uses a second MCMC implementation that differs from the one introduced in Subsection 2.1 in that it uses non-uniform brightness distribution for the exoplanet. An additional major difference is that we use as additional input the planet-star system parameter estimation from the first step of our analysis (see Subsection 2.1 + Table 1). The second MCMC algorithm models the light curve photometry by taking a brightness distribution based on simple analytic brightness models (see below) and then integrates the exoplanet flux. Approximations in the model include: ignoring the time variability of the target atmosphere (in line with atmospheric models, e.g., Cooper & Showman 2005); ignoring the planet limb darkening (expected to be weak for hot Jupiters, in particular at 8 μm); and assuming HD 189733b to be tidally locked (as non-eccentric old hot Jupiters are expected to be, e.g., Fabrycky 2010).

We perform the photometry by sampling the exoplanet surface with a grid of $2N$ points in longitude (ϕ) and N points in latitude (θ). We fix $N = 100$ to mitigate numerical effects. To estimate the broad patterns of HD 189733b brightness distribution, we use toy models as;

$$\Gamma_1(\phi,\theta) = I_1 \phi_\circ^\alpha \exp[-\phi_\circ^\beta] \cos^\gamma \theta_\circ + I_0, \quad (2)$$

$$\Gamma_2(\phi,\theta) = \begin{cases} I_1 \cos^\alpha \phi_\circ \cos^\gamma \theta_\circ + I_0 \;\; if \phi_\circ \geq 0 \\ I_1 \cos^\beta \phi_\circ \cos^\gamma \theta_\circ + I_0 \;\; if \phi_\circ < 0 \end{cases}, \quad (3)$$

$$\Gamma_3(\phi,\theta) = \begin{cases} I_1 \exp[-(\frac{\phi_\circ}{\alpha})^2] \exp[-(\frac{\theta_\circ}{\gamma})^2] + I_0 \;\; if \phi_\circ \geq 0 \\ I_1 \exp[-(\frac{\phi_\circ}{\beta})^2] \exp[-(\frac{\theta_\circ}{\gamma})^2] + I_0 \;\; if \phi_\circ < 0 \end{cases}, \quad (4)$$

where $\phi_\circ$ and $\theta_\circ$ are respectively the longitude and latitude relative to the position of the model maximum, i.e. $\phi_\circ = f(\phi, \Delta\phi, Model, \alpha, \beta, \gamma)$ and $\theta_\circ = f(\theta, \Delta\theta, Model, \alpha, \beta, \gamma)$. $\Delta\phi$ and $\Delta\theta$ are respectively the longitudinal and the latitudinal shift of the peak model from the substellar point. α, β and γ constrain the model extension. Our toy models add to traditional MCMC algorithm five jump parameters ($\Delta\phi, \Delta\theta, \alpha, \beta, \gamma$) and two linear coefficients (I_1, I_0), respectively to the amplitudes of a "hot/cold spot" mode ($\Gamma_i(\phi,\theta) - I_0$) and the constant mode (I_0).

At each step of the MCMC, we first model the target orbits and the model light curves. We then derive the mode amplitudes using the SVD method.

Note that we use three separate models in order to mitigate the model-dependence of our results. As discussed in Sec. 3, each of the models lead to similar conclusions regarding the constraint on the eccentricity-brightness degeneracy and the major patterns of the HD 189733b brightness distribution.

3. Results

Non-uniform brightness from occultation ingress/egress deviation.

Our first result is a robust, 5-σ detection of the occultation ingress/egress deviation from the eclipse scanning of a uniformly bright disk. This result was introduced in Subsection 2.1. Our upper limit on eccentricity combined with the spherical planet limit (based on a uniform transit ingress/egress), means that the occultation ingress/egress anomaly is mainly due to a non-uniform brightness distribution. On it's own the anomaly detected in occultation ingress and egress separately provide an average brightness distribution in slices on the planet as shown in Figure 1, however it does not constrain the brightness distribution in a 2D fashion.

We test the robustness of the occultation ingress/egress anomaly detection against various effects including the baseline models and the limb darkening. In particular we also validate the result's independence to subsets of AORs by analyzing different subsets of the eight eclipses. The different MCMC simulations show that there is no effect to within 1 σ.

Dominant features in a 2D brightness distribution at 8 μm

We have extracted a major spatial feature in HD 189733b brightness distribution, that corresponds to a hot spot. There is a double asymmetry in North-South ($17 \pm 10°$) and East-West ($24 \pm 11°$) within the brightness distribution. Figure 3, left panel, shows the extracted HD 189733b large-scale relative brightness (i.e. over the average host star one) distribution in the *Spitzer*/IRAC 8 μm channel. The brightness distribution in Figure 3 is the mean of the brightness distribution trials accepted along the MCMC simulation. Based on these brightness distribution trials, we also estimate the dayside standard deviation to be about 0.025 in terms of relative brightness.

In order to mitigate the model-dependence of our results, we use the three brightness models described in Subsection 2.2. All lead to the same conclusion: a brighter pattern to the North-East of the sub-stellar point and an eccentricity close to zero. In addition, our error bars are in agreement with our estimate of the brightness peak localization uncertainties reachable, about a dozen degrees in longitude and latitude, with current data quality. We obtained this estimate in analysing simulated data.

We hesitate to call the results a 2D map, because due to the limited data or data quality, we must use very simple models which average the brightness distribution over large spatial scales. In other words, there is a degeneracy in the brightness anomaly distribution; the large feature in Figure 3 could in the future be spatially resolved into more complex structures. For the reason of limited data and geometry, the interpretation of Figure 3 has to focus on global trends, in particular: the presence of an asymmetrical hot spot.

We present actually a time average large-scale brightness distribution of HD 189733b in Figure 3, left panel. In other words, Figure 3 shows the global pattern of HD 189733b brightness distribution based on eight snapshots taken from November 2005 to June 2008. We focus this discussion on the HD 189733b dayside, as it actually results of the combination of both the phase curve and the occultations. HD 189733b dayside presents an offset hot spot. The eastward shifted distribution is in agreement with the literature: (1) with previous derivations, from HD 189733b phase curve (Knutson et al. 2007) and an eclipse timing constraint (Agol et al. 2010); and (2) atmospheric models suggesting a super-rotating equatorial jet (e.g., Showman et al. 2009). In opposition, the north-south asymmetry is new. As we use large-scale, simple models to constrain the HD 189733b brightness distribution, the small-scale origin of this latitudinal asymmetry remains unconstrained. For example, a hot spot shifted to the East with a cold spot shifted to the South-West could mimic, within the current quality data, the photometry of our estimate of HD 189733b large-scale brightness distribution. In addition, such a brightness distribution could also interestingly induce the specific feature observed in Knutson et al. (2007) phase curve that is the phase curve extrema located between the transit and the occultation. To explore further this possibility and test the significance of more complex distribution we run additional MCMC simulations. These simulations use brightness models combining two of the simple brightness models introduced in Subsec. 2.2 (i.e. two hot/cold zones). Their estimate of HD 189733b large-scale brightness distribution are in excellent agreement with our results based on single "hot/cold spot" models. This confirms the low significance of small-scale pattern in current data and strengthen our previous results.

Constraint on the HD 189733b orbital eccentricity

Our work also yielded new system parameters in good agreement (to within less than 1-σ) with previous work (e.g., Triaud et al. 2009; Agol et al. 2010). Notably, we refine the upper limit for the HD 189733b eccentricity: $e \leq 0.0081$ (95% confidence). Figure 3, right panel, presents the marginal posterior density distribution of $e\cos\omega$ and $e\sin\omega$ for our two analysis steps. The dashed lines refer to the first step using a uniform disk eclipse model, the solid lines to the second step based on the non-uniform brightness models. Figure 3, right panel, highlights our degeneracy "lift" between the eccentricity (especially $e\cos\omega$, see Sec. 2.2) and the brightness distribution of an exoplanet.

By a comparison with the uniform disk eclipse model, we see the "uniform timing offset", as a shift of $e\cos\omega$ but no significant change in the $e\sin\omega$ distribution. We note that the uniform disk eclipse model estimation of $e\cos\omega$ and $e\sin\omega$, while not used for the results, are in agreement with the literature (see e.g., Triaud et al. 2009).

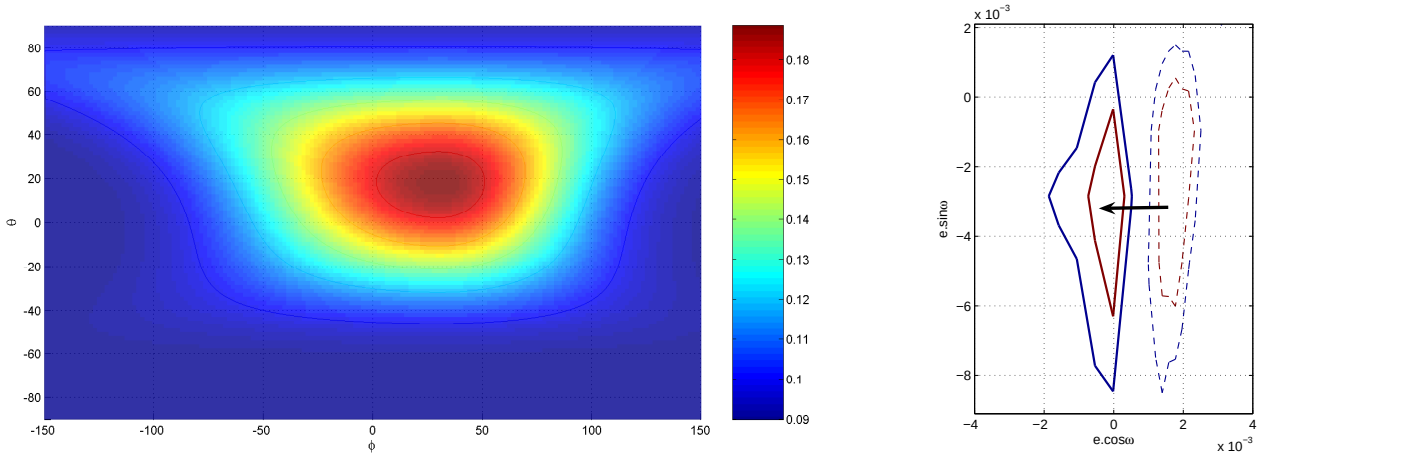

Fig. 3. Simultaneous estimation of HD 189733b global brightness distribution in IRAC 8 μm channel and eccentricity. **Left:** HD 189733b large-scale relative brightness distribution in IRAC 8 μm channel (estimated standard deviation in dayside: 0.025). **Right:** Marginal posterior density probability distribution (68.3% and 95% confidence intervals) of $e\cos\omega$ and $e\sin\omega$ for the uniform brightness case (see Sec. 2.1; *dashed line*) and the non-uniform brightness case (see Sec. 2.2; *solid line*).

4. Summary and Discussion

4.1. Methods and results

We have performed a two-step analysis of the HD 189733b public eclipses obtained at 8 μm with *Spitzer*/*IRAC*. First, we have determined the system parameters using for occultation a uniform disk eclipse model. This has led to the detection at the 5σ level of occultation ingress/egress shapes that deviate from the ingress/egress of a uniform brightness disk. We have listed as major possible origins of these shapes, the exoplanet shape, brightness distribution or eccentricity. Based on the transits residuals we have rejected the exoplanet shape as possible origin. Then, we have simultaneously analyzed our detection with HD 189733b phase curve from Knutson et al. (2007) to disentangle the contributions from the exoplanet brightness distribution in one hand and its eccentricity in the other hand. Our global analysis approach aims at mitigating the effects of systematics on individual analysis and at constraining consistently degeneracies approached previously with strong assumptions. As a result, we have derived a highly precise upper limit on HD 189733b eccentricity and have estimated its large-scale brightness distribution in IRAC 8 μm channel. This one indicates a hot spot within the atmospheric layers probed as well as a double hemispheric asymmetry. As we have used large-scale, simple models to constrain the HD 189733b brightness distribution, the small-scale origin of this latitudinal asymmetry remains unconstrained because of the data quality and the planet orbit geometry.

4.2. Comparison with Majeau et al. (2012)

We obtain qualitatively similar results as M12: an offset hot spot. Moreover, the estimations of the brightness distribution peak location are in good agreement (within less than 1σ). We recall the main difference between both studies: in our work, 1) we propagate the system parameter uncertainties; 2) we do not constrain the orbital eccentricity to zero but estimate it simultaneously with the brightness distribution; 3) the starting point of our estimation of HD 189733b brightness distribution is its 5σ eclipse scanning.

These approach differences lead to: 1) a significant difference in the estimated uncertainty on the brightness peak longitude, 21.8 ± 1.5°E compared to our 24 ± 11°E; 2) different latitudinal offset significance, 3.1 ± 9.4°N compared to our 17 ± 10°N. First, as introduced in Sec. 3 our error bars are consistent with our estimate of the brightness peak location uncertainty reachable with current data quality. Second, both M12's analysis and ours agree on the significant information of a latitudinal offset within the occultation ingress/egress: 13 ± 14.1°N (see M12 Figures 1 and 3) compared to our 17 ± 10°N. However, in M12 the significance of this latitudinal offset decreases from 13 ± 14.1°N to 3.1 ± 9.4°N when combined with the longitudinal information from the phase curve.

4.3. Future

Mapping distant worlds is a tremendous perspective that would dramatically improve our understanding of (exo)planets. As previously introduced, observations of transiting exoplanets are sensitive to both their shape and their brightness distribution. In addition, the atmospheric layers actually scanned during occultation ingress/egress are wavelength-dependent. For that reason, with additional high quality occultation photometry at different wavelength we could improve our constraint on the brightness-eccentricity degeneracy and assess the stratified structure of an exoplanet atmosphere (e.g. higher wavelength, closer to the substellar point and less extended hot spot).

In addition the time variability of these spatial features could also be targeted. Indeed, as discussed in Rauscher et al. (2007), *JWST*/NIRspec performance should allow high significance detection of modified occultation ingress/egress shapes based on a unique eclipse (for the grating centred at 4μm). The time variability would then be asses from brightness derived from different occultations.

In conclusion, the long-term challenge of constraining the exoplanet brightness distribution could ultimately lead to time-dependent three-dimensional map of distant worlds.

Acknowledgements. This work is based on observations made with the Spitzer Space Telescope, which is operated by the Jet Propulsion Laboratory, California Institute of Technology, under contract to NASA. We thank the people who made and keep the Spitzer Space Telescope such a wonderful scientific and human adventure. We thank H. Knutson for sharing HD 189733b phase curve data and discussions. JdW acknowledges the hospitality of the Institut d'Astrophysique et de Géophysique, Université de Liège where portions of this work were completed and thanks A. Lanotte and S. Sohy for their help. JdW also acknowledges support from the Grayce B. Kerr Foundation and the W.B.I. in the form of fellowships.

References

Agol, E., Cowan, N. B., Knutson, H. A., et al. 2010, ApJ, 721, 1861
Barnes, J. W., Cooper, C. S., Showman, A. P., & Hubbard, W. B. 2009, ApJ, 706, 877
Bouchy, F., Udry, S., Mayor, M., et al. 2005, A&A, 444, L15
Carter, J. A. & Winn, J. N. 2010, ApJ, 709, 1219
Charbonneau, D., Knutson, H. A., Barman, T., et al. 2008, ApJ, 686, 1341
Claret, A. & Bloemen, S. 2011, A&A, 529, A75
Cooper, C. S. & Showman, A. P. 2005, ApJ, 629, L45
Deming, D., Harrington, J., Seager, S., & Richardson, L. J. 2006, ApJ, 644, 560
Deroo, P., Swain, M. R., & Vasisht, G. 2010, ArXiv e-prints
Désert, J.-M., Lecavelier des Etangs, A., Hébrard, G., et al. 2009, ApJ, 699, 478
Dobbs-Dixon, I., Cumming, A., & Lin, D. N. C. 2010, ApJ, 710, 1395
Fabrycky, D. C. 2010, Non-Keplerian Dynamics of Exoplanets, ed. Seager, S., 217–238
Fazio, G. G., Hora, J. L., Allen, L. E., et al. 2004, ApJS, 154, 10
Ford, E. B. 2006, ApJ, 642, 505
Gillon, M., Demory, B.-O., Triaud, A. H. M. J., et al. 2009, A&A, 506, 359
Gillon, M., Hatzes, A., Csizmadia, S., et al. 2010a, A&A, 520, A97
Gillon, M., Lanotte, A. A., Barman, T., et al. 2010b, A&A, 511, A3
Gregory, P. C. 2005, Bayesian Logical Data Analysis for the Physical Sciences: A Comparative Approach with 'Mathematica' Support, ed. Gregory, P. C. (Cambridge University Press)
Grillmair, C. J., Charbonneau, D., Burrows, A., et al. 2007, ApJ, 658, L115
Horne, K. 1985, MNRAS, 213, 129
Knutson, H. A., Charbonneau, D., Allen, L. E., et al. 2007, Nature, 447, 183
Knutson, H. A., Charbonneau, D., Cowan, N. B., et al. 2009, ApJ, 690, 822
Madhusudhan, N. & Seager, S. 2009, ApJ, 707, 24
Majeau, C., Agol, E., & Cowan, N. 2012, ArXiv e-prints
Mandel, K. & Agol, E. 2002, ApJ, 580, L171
Moses, J. I., Visscher, C., Fortney, J. J., et al. 2011, ApJ, 737, 15
Press, W. H., Flannery, B. P., Teukolsky, S. A., & Vetterling, W. T. 1992, Numerical Recipes in FORTRAN: The Art of Scientific Computing, 2nd ed. (Cambridge University Press), 51–63
Rauscher, E. & Menou, K. 2010, ApJ, 714, 1334
Rauscher, E., Menou, K., Seager, S., et al. 2007, ApJ, 664, 1199
Redfield, S., Endl, M., Cochran, W. D., & Koesterke, L. 2008, ApJ, 673, L87
Seager, S. & Deming, D. 2010, ARA&A, 48, 631
Showman, A. P., Fortney, J. J., Lian, Y., et al. 2009, ApJ, 699, 564
Showman, A. P. & Guillot, T. 2002, A&A, 385, 166
Southworth, J. 2010, MNRAS, 408, 1689
Stetson, P. B. 1987, PASP, 99, 191
Swain, M. R., Vasisht, G., & Tinetti, G. 2008, Nature, 452, 329
Tinetti, G., Vidal-Madjar, A., Liang, M.-C., et al. 2007, Nature, 448, 169
Triaud, A. H. M. J., Queloz, D., Bouchy, F., et al. 2009, A&A, 506, 377
Warner, B., Robinson, E. L., & Nather, R. E. 1971, MNRAS, 154, 455
Werner, M. W., Roellig, T. L., Low, F. J., et al. 2004, ApJS, 154, 1

Williams, P. K. G., Charbonneau, D., Cooper, C. S., Showman, A. P., & Fortney, J. J. 2006, ApJ, 649, 1020
Winn, J. N. 2010, Exoplanet Transits and Occultations, ed. Seager, S., 55–77
Winn, J. N., Holman, M. J., Torres, G., et al. 2008, ApJ, 683, 1076

Table 2. AOR's description

AORKEY($\bigoplus$[a])	**PI**	**Publication Ref.**	**Datasets**[b] (64x)	**Exposure time [s]**	**Aperture [px]**
16343552(O)	D. Charbonneau	Charbonneau et al. (2008)	1359	0.1	3.6
20673792(P)	D. Charbonneau	Knutson et al. (2007)	1319	0.4	4.8
22808832(O)	E. Agol	Agol et al. (2010)	690	0.4	4.8
22809088(O)					
22809344(O)					
22810112(O)					
24537600(O)					
27603456(O)					
22807296(T)	E. Agol	Agol et al. (2010)	690	0.4	4.8
22807552(T)					
22807808(T)					
24537856(T)					
27603712(T)					
27773440(T)					

[a] AORKEY target: T, O or P respectively transit, occultation or phase-curve.
[b] Present AOR are composed of datasets, each dataset corresponds to 64 individual subarray images of 32x32 px.